AIAA JOURNAL
Vol. 40, No. 8, August 2002

Application of Large-Eddy Simulation to Supersonic Compression Ramps

Donald P. Rizzetta* and Miguel R. Visbal†
U.S. Air Force Research Laboratory, Wright–Patterson Air Force Base, Ohio 45433-7512

Large-eddy simulations of supersonic compression-ramp flowfields were performed by a high-order numerical method, utilizing the Smagorinsky dynamic subgrid-scale model to account for spatially underresolved stresses. Computations were carried out at a freestream Mach number of 3.0 for ramp angles of 8, 16, 20, and 24 deg. Extensive comparisons are made between the respective solutions and available experimental data that were collected at higher Reynolds numbers. These include surface pressure, skin friction, and both mean and fluctuating velocity profiles. For the 24-deg case, a number of experimentally measured statistical quantities are compared to the simulation.

Nomenclature

C_f	=	time-mean skin-friction coefficient
C_p	=	time-mean surface pressure coefficient, $2(p_{wm} - p_\infty)/\rho_\infty u_\infty^2$
E_k	=	normalized spanwise turbulence kinetic energy spectra
K	=	time-mean turbulence kinetic energy
Ku	=	kurtosis of wall pressure
k_3	=	nondimensional wave number in z direction
L_x, L_y, L_z	=	nondimensional domain extents
l	=	dimensional reference length
M_∞	=	freestream Mach number
p	=	nondimensional static pressure
Re	=	reference Reynolds number, $\rho_\infty u_\infty l/\mu_\infty$
Re_δ	=	boundary-layer thickness Reynolds number
Re_θ	=	momentum thickness Reynolds number
Sk	=	skewness of wall pressure
s	=	normalized standard deviation of wall pressure
T	=	nondimensional static temperature
u, v	=	nondimensional Cartesian velocity components in x, y directions
u_n	=	nondimensional velocity component normal to wall surface
u_t	=	nondimensional velocity component tangential to wall surface
X	=	nondimensional coordinate tangential to wall surface, origin at the corner
x, y, z	=	nondimensional Cartesian coordinates in the streamwise, vertical, and spanwise directions
Y	=	nondimensional coordinate normal to wall surface, origin at the surface
Γ	=	intermittency of wall pressure
Δt	=	nondimensional time-step size
$\Delta x, \Delta y, \Delta z$	=	mesh step sizes
δ	=	nondimensional boundary-layer thickness
δ^*	=	nondimensional boundary-layer displacement thickness
θ	=	nondimensional boundary-layer momentum thickness
ρ	=	nondimensional fluid density
ϕ	=	compression-ramp angle

Subscripts

e	=	evaluated at the boundary-layer edge
i	=	inviscid value
m	=	time-mean value
w	=	evaluated at the wall
0	=	evaluated at the inflow location
1	=	evaluated upstream of interaction

Superscripts

$\sim$	=	Favre-averaged component
$'$	=	fluctuating component
$+$	=	value given in law-of-the-wall units

Introduction

ADVANCES in the accuracy of numerical algorithms and the speed and storage capacity of computing machinery have made it possible to perform direct numerical simulation (DNS) for a restricted class of turbulent flowfields. Because such simulations are characterized by severe resolution requirements, particularly near wall-bounded regions, they are currently limited to relatively low Reynolds numbers and to geometrically simple configurations. For somewhat more practical applications, such computations can be extended through the use of large-eddy simulation (LES). This is accomplished in LES by leaving small-scale fluid structures spatially underresolved and accounting for them by means of a subgrid-scale (SGS) turbulence model. Although DNS and LES have quite general applicability, until recently, the majority of flows considered by these methods have been incompressible or subsonic.

LES of supersonic flows is useful for studying compressibility effects, which can alter the fluid physics. Such studies increase the understanding of turbulence mechanisms and can lead to the development, improvement, and testing of lower-order closure models. Despite remaining computationally intensive, LES also may be beneficial in the design and analysis of high-speed flight vehicles and associated propulsion systems where less sophisticated approaches fail.

A number DNS and LES have been generated for flat-plate flowfields. These include the spatially evolving boundary layer at a Mach number of 2.25 and $Re_\theta \approx 6000$, which was considered in the DNS of Rai et al.[1] and the corresponding LES of Spyropoulos and Blaisdell[2] employing the Smagorinsky dynamic SGS model.[3] Both of these simulations utilized a fifth-order-accurate upwind-biased finite difference description of inviscid fluxes. A similar LES of this

Presented as Paper 2001-2858 at the AIAA 31st Fluid Dynamics Conference, Anaheim, CA, 11–14 June 2001; received 16 July 2001; revision received 14 February 2002; accepted for publication 14 February 2002.

*Senior Research Aerospace Engineer, Computational Sciences Branch, Aeronautical Sciences Division. Associate Fellow AIAA.

†Technical Area Leader, Computational Sciences Branch, Aeronautical Sciences Division. Associate Fellow AIAA.

same flow was obtained by Rizzetta et al.[4] using a high-order compact scheme. By making an approximate spatial growth treatment, Guarini et al.[5] produced the direct simulation for a Mach 2.5 boundary layer. The DNS of Lee et al.[6] and LES of Ducros et al.[7] have also been used to examine interactions of isotropic turbulence with a normal shock wave that was relatively weak.

Supersonic compression-ramp flowfields have been studied extensively, both experimentally and computationally, due to their geometric simplicity. Large-scale shock wave oscillations at a frequency that was found to correlate with the bursting phenomenon of the upstream boundary layer were observed by Andreopoulos and Muck.[8] Smits and Muck[9] obtained detailed measurements of the fluctuating flowfield that confirmed that observation. Experiments performed by Dolling and Murphy[10] at a Mach number of 3.0, however, detected shock wave motion that was random. This result was verified by Dolling and Or,[11] who noted that incipient separation occurred for a ramp angle of 16 deg. Further observations by Erengil and Dolling[12,13] concluded that the shock motion contains both large-scale and small-scale fluctuations, and whereas these oscillations are generally random, there is a correlation between the shock wave motion and pressure fluctuations in the upstream boundary layer.

Numerical investigations of supersonic compression-ramp flows have typically considered the Reynolds-averaged Navier–Stokes equations used in conjunction with mean turbulence models. These efforts have met with limited success in the prediction of quantities such as heat transfer and skin friction, particularly in situations with large reversed-flow regions.[14] It is believed that this difficulty may be due in part to the disparity between the time-mean and instantaneous shock-system structure. In addition, the models and resultant computations often fail to account for compressibility effects or the three dimensionality of the flowfield.

A "very large-eddy simulation" of a 24-deg compression ramp at Mach 2.8 was performed by Hunt and Nixon[15] and indicated a correlation between upstream fluctuations and shock wave motion. For the Mach 3.0 flow past an 8-deg ramp, no separation was found in the LES of Urbin et al.[16] Some preliminary results were later obtained at a ramp angle of 25 deg.[17] Adams[18,19] carried out a DNS for an 18-deg compression ramp at Mach 3.0, which indicated a small region of reversed mean flow, but no large-scale shock wave motion. This result was verified by the DNS and LES of Rizzetta et al.[4,20]

The objective of the present effort is to provide an extensive numerical investigation of supersonic compression-ramp flowfields. LES at a freestream Mach number of 3.0 are carried out for ramp angles of 8, 16, 20, and 24 deg. Details of the computations are summarized, and results for each case are compared to each other and with experimental data that were collected at higher Reynolds numbers. Both mean flow[14,21] and fluctuating measurements[9,10] are available for this purpose.

Governing Equations

The governing equations employed for the simulations are the unsteady three-dimensional compressible Favre-filtered Navier–Stokes equations. These were written in nondimensional variables and solved in conservative form. The entire set of these equations may be found in Refs. 4 and 20 and is not reproduced here.

Spatially underresolved stresses in the LES are represented by the Smagorinsky dynamic SGS model, which was first proposed by Germano et al.[3] for incompressible flows. The present computations incorporate Yoshizawa's[22] treatment of the stress tensor and extensions of the dynamic model by Moin et al.[23] for compressible applications. A comprehensive development of the model equations appears in Refs. 4 and 20.

Numerical Method

Time-accurate solutions to the governing equations were obtained numerically by the implicit approximately factored finite difference algorithm of Beam and Warming,[24] employing Newton-like subiterations,[25] which has evolved as an efficient tool for generating solutions to a wide variety of complex fluid flow problems. Spatial derivatives are represented by a compact approximation that is used in conjunction with a 10th-order nondispersive filter. Subiterations are used to achieve second-order temporal and sixth-order spatial accuracy. In the region of strong shock waves, the compact differencing of convective fluxes is replaced locally by a third-order Roe upwind-biased evaluation. References 4 and 20 provide more complete details of the numerical method.

The aforementioned features of the numerical algorithm are embodied in an existing fully vectorized, time-accurate, three-dimensional computer code FDL3DI,[26] which has proven to be reliable for steady and unsteady fluid flow problems, including the simulation of flows over delta wings with leading-edge vortices,[27–30] vortex breakdown,[28–30] DNS of transitional wall jets[31] and synthetic jet actuators,[32] and DNS and LES of subsonic[33] and supersonic flowfields.[4,20]

Details of the Computations

Reference conditions for the computations considered here are found in Table 1 and are identical to those employed for the DNS and LES of flow past an 18-deg compression ramp considered in Ref. 4. Also appearing in Table 1 are corresponding conditions for associated experimental investigations to which computations will be compared. In the results that follow, large-scale variables were decomposed into time-mean values and fluctuating components, such as, for example,

$$\tilde{u} = u_m + u' \tag{1}$$

A computational domain size was taken to be similar to that studied by Adams[18,19] and Rizzetta et al.,[4,20] which is given in terms of the mean incoming boundary-layer thickness δ_0 as

$$L_x = 31.2\delta_0, \qquad L_y = 4.7\delta_0, \qquad L_z = 2.9\delta_0 \tag{2}$$

where L_x, L_y, and L_z, are streamwise, vertical, and spanwise extents, respectively. The vertical extent L_y corresponds to the domain height at the inflow location. Grid spacing is uniform in the streamwise direction at the wall, except in the region near the corner. Beyond the streamwise extent L_x noted in Eq. (2), the mesh was rapidly stretched in the streamwise direction to the outflow boundary. This rapid stretching, in conjunction with the filter utilized by the numerical method, was employed to provide a nonreflective buffer zone. In the vertical direction at the inflow boundary, geometric stretching of the y grid lines was enforced, with a constant mesh spacing ratio of 1.017.

For each ramp angle, two-dimensional computational grids were generated in x–y planes by an elliptic solver using automated software[34] to maintain orthogonality between grid lines and at domain boundaries. The two-dimensional grids were then uniformly distributed along the span, where constant spacing and a five-grid plane overlap was employed at domain boundaries to facilitate application of periodic conditions. Dimensions of the grids for these computations were $(421 \times 151 \times 81)$ points in (i, j, k), respectively, that correspond to the streamwise, vertical, and spanwise directions. In the 24-deg case, a coarse mesh consisting of $(211 \times 76 \times 81)$ points was also constructed by removing every other grid line in the i direction. The minimum vertical spacing at the wall was maintained, and j grid lines were regenerated. At the inflow location, the

Table 1 Compression ramp flow conditions

Reference	l, m	M_∞	Re	$Re_{\delta 0}$	$Re_{\theta 0}$
Present	2.4×10^{-4}	3.00	6.5×10^3	2.08×10^4	1.696×10^3
Smits and Muck[9]	1.0	2.79–2.87	6.3×10^7	1.58×10^6–1.64×10^6	8.19×10^4
Dolling and Murphy[10]	1.0	2.90–2.95	6.5×10^7	8.13×10^5–1.44×10^6	3.86–6.91×10^4
Settles and Dodson[21]	1.0	2.84–2.87	6.3×10^7	1.45×10^6–1.64×10^6	7.56–8.19×10^4

fine grid had the following minimum spacings in wall units:

$$\Delta x^+ = 16.8, \qquad \Delta y^+ = 1.4, \qquad \Delta z^+ = 8.3 \qquad (3)$$

Based on the mean incoming profile, 79 of the 151 vertical grid points were within the boundary layer.

Inflow data for the compression-ramp simulations were obtained from a spatially evolving flat-plate simulation, which was used to produce profiles of the dependent variables. This computation itself required a separate calculation to effect transition on the plate. These profiles are identical to those used for simulations of the 18-deg ramp case computed in Refs. 4 and 20, which were generated to match Re_θ from the DNS of Adams.[18,19] A description of the development of the inflow profiles can be found in Ref. 35, along with more complete details of computed results. Mean incoming boundary-layer parameters appear in Table 2.

The spanwise averaged mean streamwise inflow velocity profile is compared to the data of Settles and Dodson[21] in Fig. 1. Because of the low Reynolds number, the slope of the computed profile in the near-wall region is not as steep as the experimental value. Corresponding profiles of the fluctuating streamwise velocity and Reynolds stress are also presented in Fig. 1. The absence of a near-wall peak in the experimental profile of the streamwise velocity is likely due to the limitation of the hot-wire probe used to take the measurements, as was indicated in Ref. 9.

For all simulations, including those used to construct inflow data, the time step was specified as $\Delta t = 0.1$. To initialize each computation, preliminary solutions were first generated on a coarse computational mesh, which was obtained by removing every other i and j grid line. These coarse-mesh solutions were interpolated to the nominal grid. Every case was then allowed to evolve for one period of the cycled inflow profiles (2267 time steps) to attain a turbulent equilibrium state. This corresponded approximately to 2.3 flow times through the streamwise extent L_x noted in Eq. (2). Solutions then continued to evolve for an additional 5.5 periods of the inflow data, corresponding to 12,469 time steps and 12.5 flow-through times, over which statistical information was recorded.

Table 2 Mean incoming boundary-layer parameters

Parameter	Value
δ_0	3.202
θ_0	0.261
δ_0^*	0.834
C_{f0}	2.634×10^{-3}
$Re_{\theta 0}$	1696

At the inflow boundary, instantaneous values obtained by the aforementioned procedure were prescribed for all dependent variables. Simple extrapolation was employed at the outflow plane downstream of the stretched-mesh region. On the solid surface, the no-slip condition was enforced together with a fourth-order-accurate representation of zero normal pressure gradient. The isothermal temperature $T = 2.522$ was also specified along this surface, corresponding to the previous computations of Adams[18,19] and Rizzetta et al.[4,20] Because the top of the computational domain was located above the shock, simple extrapolation was applied along the upper boundary. At the spanwise ends of the domain, periodicity was implemented using the overlapping grid planes.

Results

Because the LES were carried out at a Reynolds number that was considerably lower than those at which experiments were performed (Table 1), only qualitative agreement can be expected between numerical solutions and measured data. Furthermore, differences in the inflow profiles that were observed in Fig. 1 will contribute to a disparity. In the results to follow, comparison of time-mean quantities will be made with the experiment of Settles et al.,[14] which is documented in Ref. 21. Some time-mean velocities and profiles of fluctuating quantities are compared with the measurements of Smits and Muck,[9] who collected data for $\phi = 8$, 16, and 20 deg. A ramp angle of 24 deg was not considered in this experiment due to physical constraints of the data collecting system. Measurements of fluctuating surface pressure for a ramp angle of 24 deg from the investigation of Dolling and Murphy[10] is also utilized in this study. In all of the experiments, sidewall end plates were utilized at the spanwise edges of the ramp configuration, which were not modeled by the periodic conditions employed for the simulations. As noted earlier, a more comprehensive presentation of numerical results appears in Ref. 35.

Spanwise averaged time-mean surface pressure distributions are shown in Fig. 2. The pressure coefficient has been normalized by the inviscid rise, Cp_i, in each case to account for variations in the freestream Mach number between computations and experiment. An appreciable boundary-layer displacement effect occurs in the numerical solutions because of the low Reynolds number employed for the LES. This causes a rise in Cp on the flat-plate region upstream of the corner and an overall turning of the inviscid flow that is appreciably greater than the theoretical value in some cases. As the

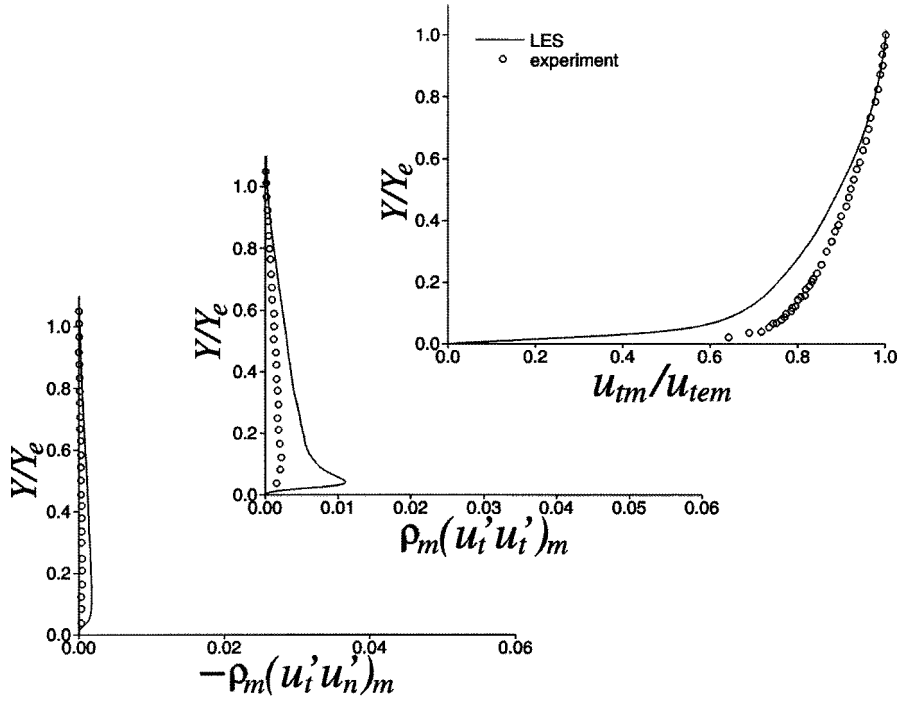

Fig. 1 Spanwise-averaged time-mean tangential velocity, fluctuating tangential velocity, and Reynolds-stress profiles for inflow.

Table 3 Separation pressure coefficients

ϕ	Cp_{sep}
16	0.060
20	0.061
24	0.064

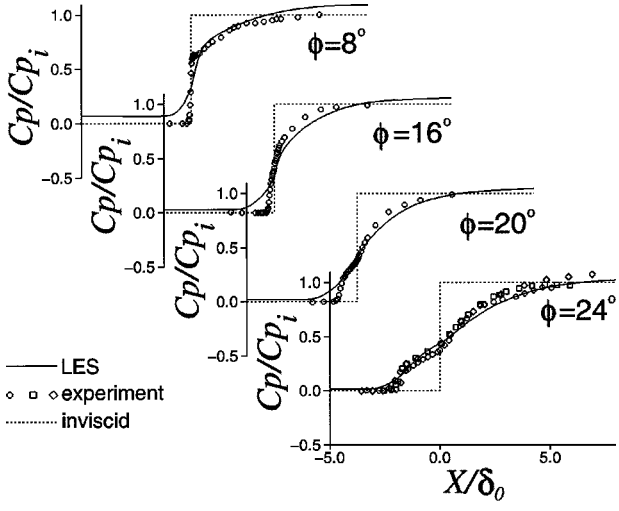

Fig. 2 Spanwise-averaged time-mean surface pressure coefficient distributions.

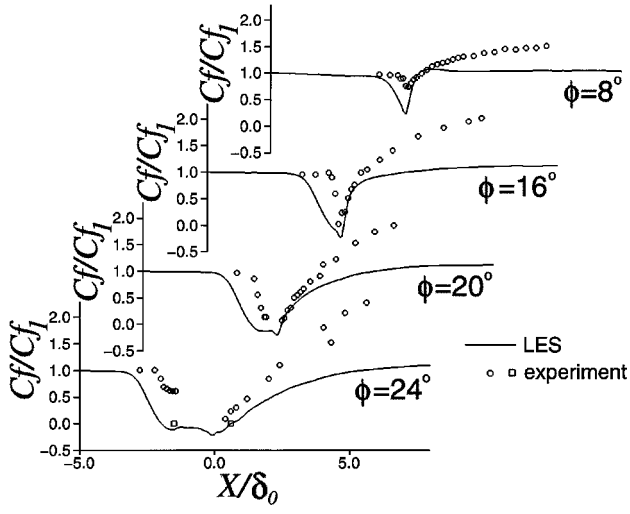

Fig. 3 Spanwise-averaged time-mean skin-friction coefficient distributions.

ramp angle increases, the turning due to boundary-layer displacement is a smaller fraction of the total turning, so that this effect is diminished. For this reason, numerical results compare more favorably with experiments at ramp angles of 20 and 24 deg than at 8 and 16 deg.

Corresponding skin-friction coefficient distributions are compared in Fig. 3. To compensate for differences in the inflow profiles between computations and measurements, Cf has been normalized by its value upstream of the interaction region, Cf_1. In all cases, the streamwise extent of the interaction is greater for the numerical solutions than it is for the experiments because the Reynolds number is lower (see Ref. 36, Fig. 3.62). The downstream rise of the skin friction that is evident in the experimental data is not present in the computations.

Values of the time-mean pressure coefficient at the separation location have been recorded in Table 3. Although a slight rise in Cp_{sep} is noted for increasing ramp angle, its approximately constant value confirms the self-induced separation concept of Delery.[37]

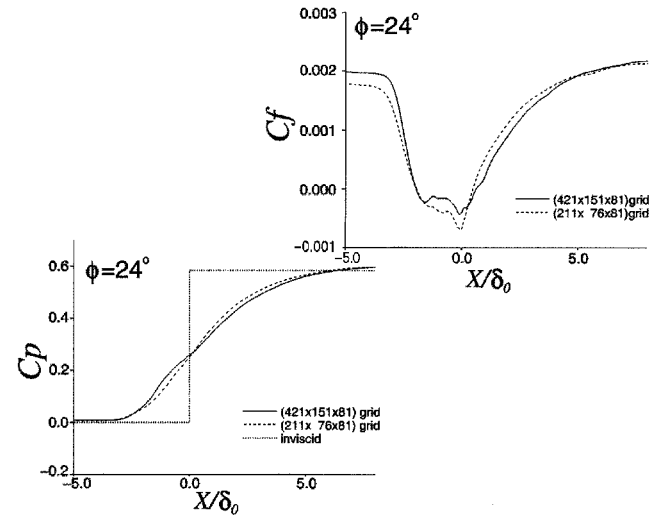

Fig. 4 Effect of grid resolution on spanwise-averaged time-mean surface pressure and skin-friction coefficient distributions for 24-deg compression ramp.

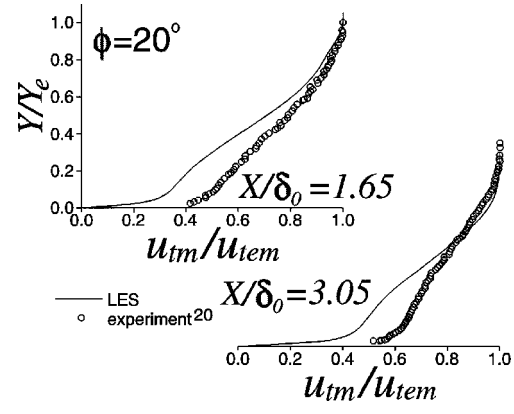

Fig. 5 Spanwise-averaged time-mean tangential velocity profiles for 20-deg compression ramp.

Because of the extensive computational resources required to perform these simulations, a comprehensive grid resolution study could not be performed. Additionally, although there exists no concept of grid independence for LES in the absence of explicit filtering,[38] it is beneficial to carry out coarse-grid computations for the purpose of determining their suitability for practical applications. Figure 4 illustrates the effect of grid resolution for the 24-deg ramp-angle case on the surface pressure and skin-friction coefficients. Here, the coefficients have not been normalized as was done earlier, so that the effect of grid refinement may be more directly assessed. Although reasonable results are still obtained in the coarse-grid solution, some loss of accuracy is apparent. In particular, the small pressure plateau region near the corner is less well defined in Fig. 4.

Profile information normal to the wall surface for all ramp angles is presented in Figs. 5–11. Seen in Figs. 5 and 6 are spanwise averaged time-mean velocity profiles at two representative streamwise locations downstream of the corner. Also provided are the data of Settles and Dodson.[21] Although the measured and computed results are qualitatively similar, the LES profiles are much less full than their experimental counterparts in all cases. This is because the incoming upstream numerical profiles were less full, and the Reynolds number is much lower.

Profiles of the spanwise averaged time-mean fluctuating tangential velocity are indicated in Figs. 7 and 8, along with the data of Smits and Muck.[9] Whereas a near-wall peak in the profiles is absent in the experiment, the comparison with computations for ramp

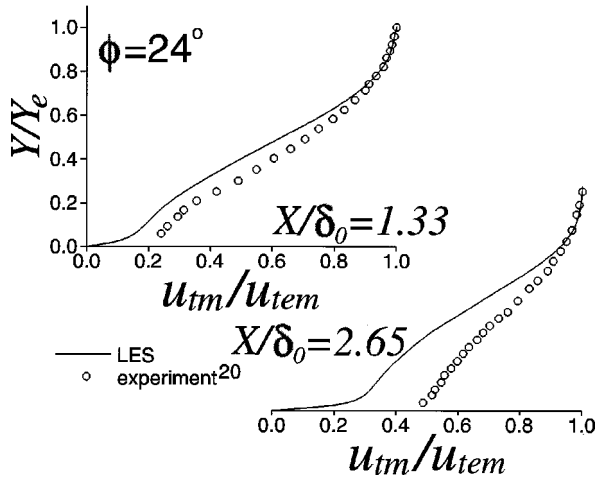

Fig. 6 Spanwise-averaged time-mean tangential velocity profiles for 24-deg compression ramp.

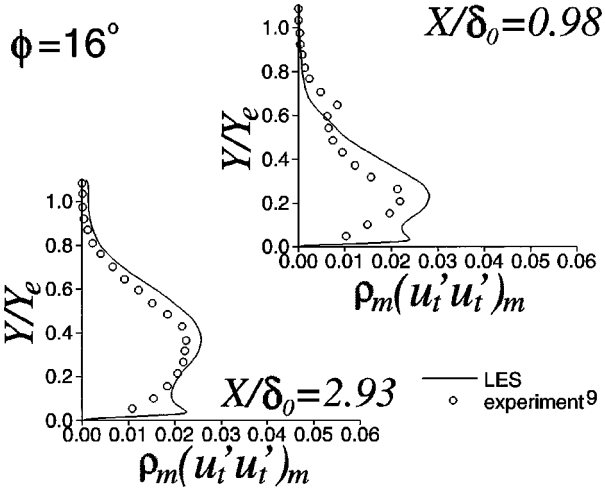

Fig. 7 Spanwise-averaged fluctuating tangential velocity profiles for 16-deg compression ramp.

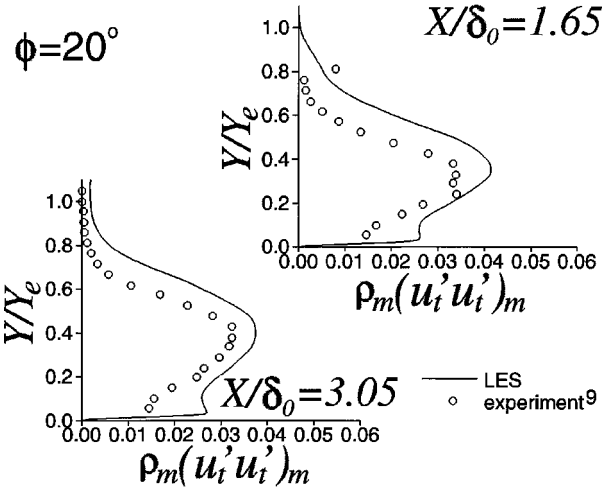

Fig. 8 Spanwise-averaged fluctuating tangential velocity profiles for 20-deg compression ramp.

angles of 16 and 20 deg is generally favorable. Reynolds stress profiles are found in Figs. 9 and 10. Here, the disparity between the simulations and the measurements is considerable. In addition to a near-wall peak, the numerical results attain much higher levels than the experimental data. With reference to Fig. 1, a similar disparity was found in the inflow Reynolds stress profiles.

Spanwise-averaged time-mean turbulent kinetic energy profiles for all ramp angles are shown in Fig. 11, where

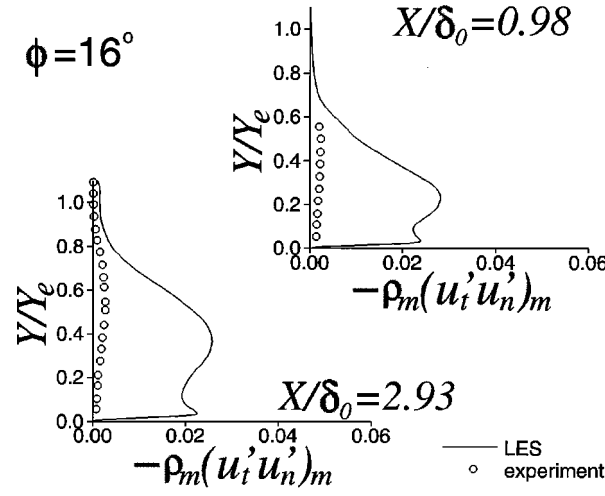

Fig. 9 Spanwise-averaged fluctuating Reynolds-stress profiles for 16-deg compression ramp.

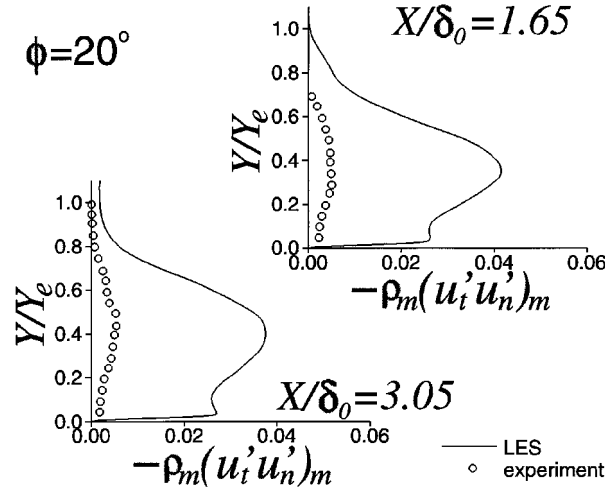

Fig. 10 Spanwise-averaged fluctuating Reynolds-stress profiles for 20-deg compression ramp.

$$K = (u'u' + v'v' + w'w')_m \tag{4}$$

As expected, the turbulence energy level increases with increasing ramp angle due to the adverse pressure gradient incurred by streamline curvature and by increasing shock strength.

Comparisons of computed surface pressure fluctuations with the data of Dolling and Murphy[10] for $\phi = 24$ deg are made in Figs. 12–16. The normalized wall pressure standard deviation is calculated as

$$s = \left(\frac{1}{p_{wm1}}\right)\left[\sum_{n=1}^{N}\frac{p_w^n - p_{wm}}{N-1}\right]^{\frac{1}{2}} \tag{5}$$

and appears in Fig. 12. Here, N is the total number of samples that corresponds to one per time step in the present case ($N = 12{,}469$) and p_{wm1} is the mean wall pressure just upstream of the interaction. The value of s upstream of the interaction (s_1) has been removed from the standard deviation to account for differences in the incoming states between the computation and the experiment. Apart from the disparity near separation ($X/\delta_0 \approx -2.0$), the comparison is quite favorable. The disparity is caused by differences in the shock wave motion between the respective results, which will be illustrated subsequently.

Presented in Figs. 13 and 14 are the wall pressure skewness and kurtosis, defined, respectively, as

$$Sk = \left(\frac{1}{Ns^3}\right)\sum_{n=1}^{N}\left(p_w^n - p_{wm}\right)^3 \tag{6}$$

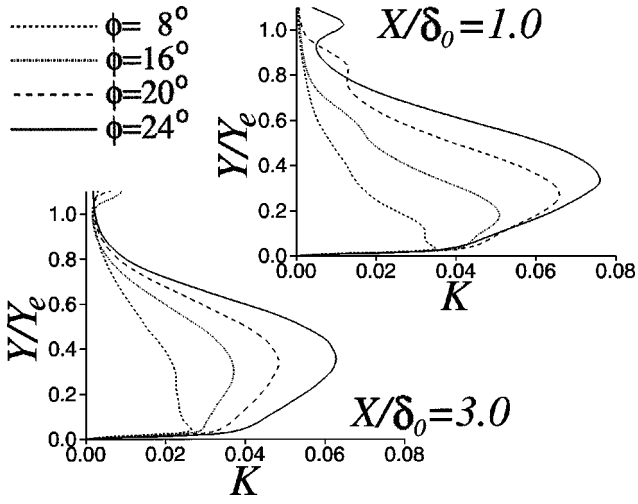

Fig. 11 Spanwise-averaged time-mean turbulent kinetic energy profiles for 8-, 16-, 20-, and 24-deg compression ramps.

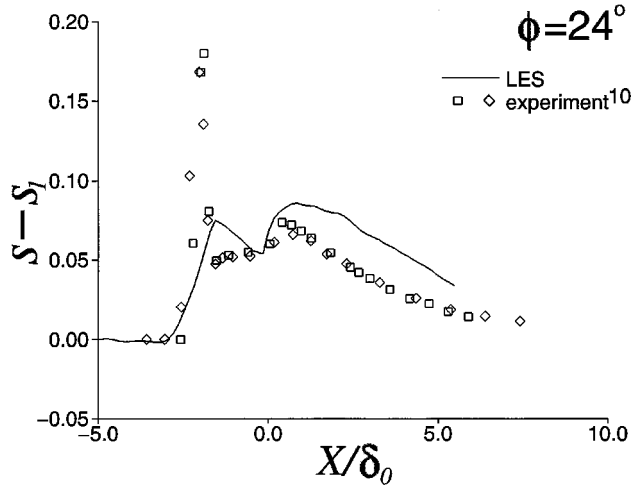

Fig. 12 Spanwise-averaged surface pressure standard deviation distribution for 24-deg compression ramp.

$$Ku = \left(\frac{1}{Ns^4}\right)\sum_{n=1}^{N}\left(p_w^n - p_{wm}\right)^4 \tag{7}$$

The computed skewness seen in Fig. 13 is much like that of the experiment, except, once again, for the sharp peak near separation. Somewhat more disparity occurs in the kurtosis. Differences in the upstream state are apparent.

The wall pressure intermittency is displayed in Fig. 15, where Γ is designated by Dolling and Murphy[10] as the fraction of time that the flowfield is in an undisturbed state. The quantity is defined as

$$\Gamma = \frac{\text{time}[p_w > (p_{wm1} + 3s_1)]}{\text{total time}} \tag{8}$$

It is observed in Fig. 15 that the experimental distributions have a steeper rise that occurs farther downstream than the numerical result. This is due to the more extensive interaction region of the low Reynolds number LES.

Instantaneous surface pressure time histories are compared in Fig. 16 at a location near the time-mean separation point. The timescale of Dolling and Murphy[10] has been nondimensionalized using the freestream velocity and the boundary-layer thickness to compare to the computed result. Mean pressure values of the two distributions are in good agreement, as was demonstrated by Fig. 2. The fluctuating components, however, indicate very different shock motion in each case. High-frequency oscillations exhibited in the numerical simulation are quite similar to those of the incoming boundary layer, thus signifying no large-scale shock excursions.

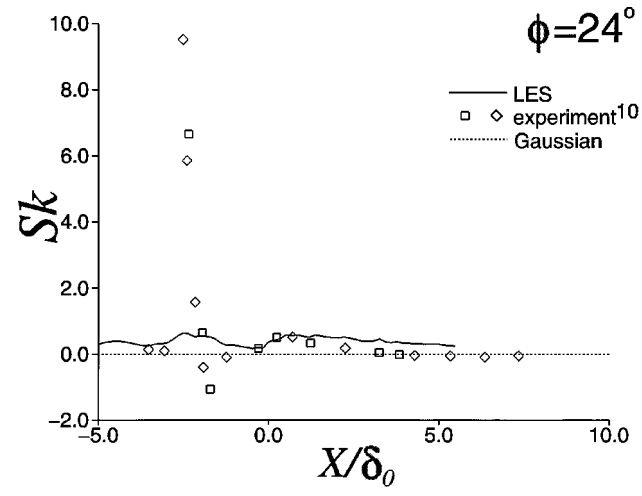

Fig. 13 Spanwise-averaged surface pressure skewness distribution for 24-deg compression ramp.

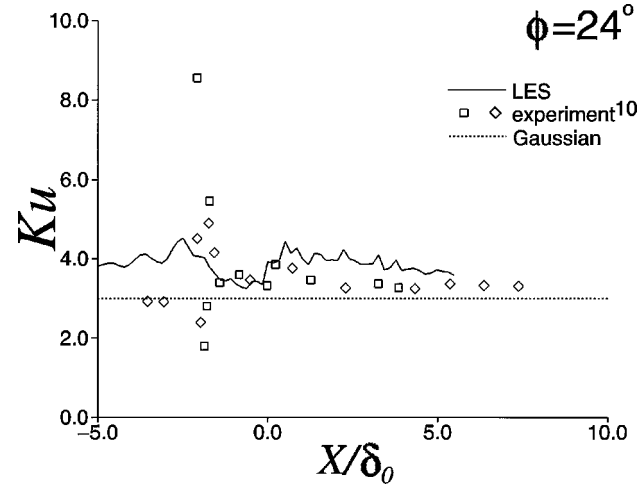

Fig. 14 Spanwise-averaged surface pressure kurtosis distribution for 24-deg compression ramp.

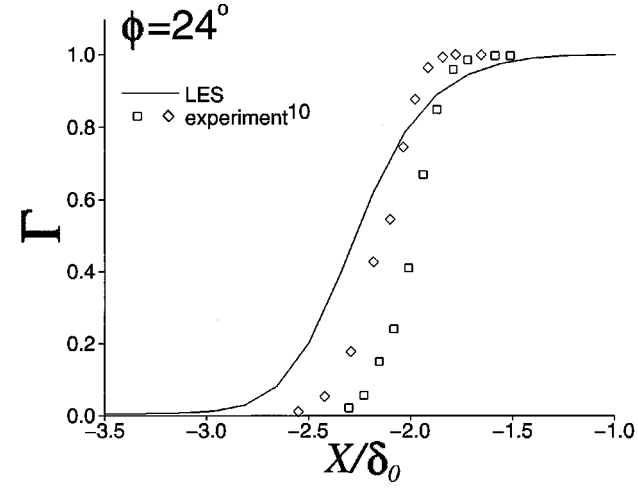

Fig. 15 Spanwise-averaged surface pressure intermittency distribution for 24-deg compression ramp.

This pressure time history is much like the DNS of Adams[19] for an 18-deg compression ramp. By contrast, the low-frequency modes of the experimental distribution represent extensive movement of the shock, where the time between crossings of the mean value line is proportional to the distance traveled.

Spanwise turbulent kinetic energy spectra at $X/\delta_0 = 2.1$ and $Y/\delta_0 = 0.5$ for all ramp angles are provided in Fig. 17. In Fig. 17, instantaneous spectra have been temporally averaged, and E_k has

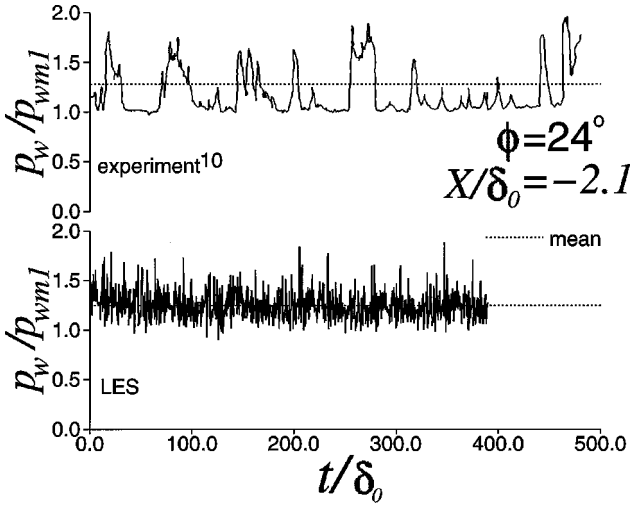

Fig. 16 Midspan surface pressure time history at $X/\delta_0 = -2.1$ for 24-deg compression ramp.

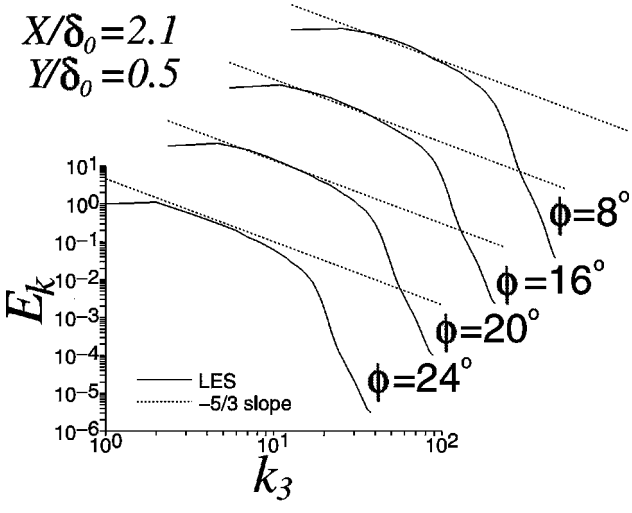

Fig. 17 Spanwise turbulent kinetic energy spectra at $X/\delta_0 = 2.1$ and $Y/\delta_0 = 0.5$ for 8-, 16-, 20-, and 24-deg compression ramps.

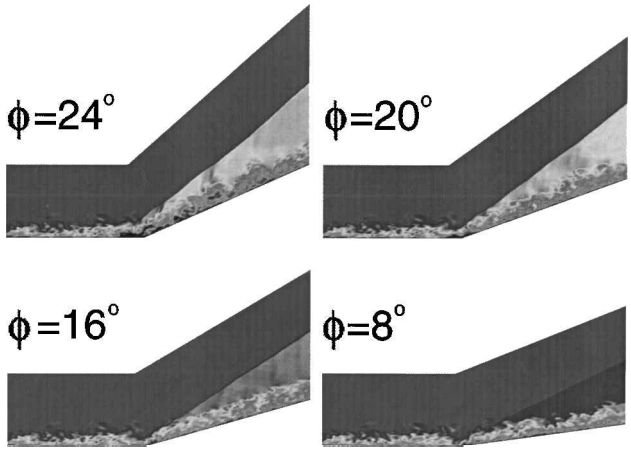

Fig. 18 Instantaneous Mach number contours at midspan location for 8-, 16-, 20-, and 24-deg compression ramps.

been normalized by its value at $k_3 = 1$. Little dependence on ramp angle is evident.

Found in Fig. 18 are instantaneous Mach number contours at the midspan location for all four ramp angles. It can be seen that the postshock Mach number in the inviscid portion of the flowfield decreases as the compression ramp angle increases, as expected. Regions of low-speed flow in the corner region are apparent, the extent of which increases with increasing ramp angle. A close inspection of

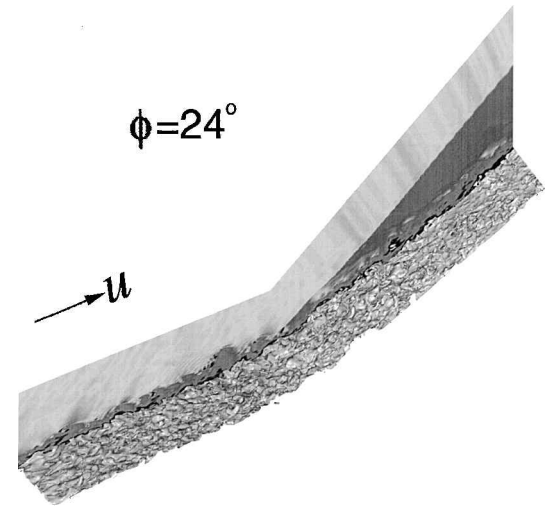

Fig. 19 Instantaneous total pressure coefficient contours at the spanwise boundary and isosurface for 24-deg compression ramp.

Fig. 18 evidences that the normal extent of the large-scale structures increases with increasing ϕ. Presented in Fig. 19 are instantaneous total pressure coefficient contours at the spanwise boundary and an isosurface. The level of the isosurface corresponds to a value of the total pressure coefficient near the outer edge of the boundary layer. The intermittent nature of the boundary-layer edge is apparent.

Summary

A high-order finite difference method was used to perform LES of the Mach 3.0 flow past compression ramps of 8, 16, 20, and 24 deg. Spatial derivatives were represented by a 6th-order compact scheme that was used in conjunction with a 10th-order nondispersive filter. The inviscid regions immediately surrounding shock waves were treated by a third-order Roe upwind-biased evaluation of the convective fluxes. Spatially underresolved stresses in the large-eddy formulation were accounted for by the Smagorinsky dynamic subgrid model.

Extensive comparisons were made between numerical simulations and experimental data. It should be emphasized, however, that significant differences existed in these respective investigations. Notable among these was the Reynolds number, which was two orders of magnitude greater in the experiment. The experimental configuration employed sidewall end plates, which were not modeled in the computations. In addition, nondimensional incoming profiles used in the simulations could not duplicate those of the experiment.

Computed time-mean surface pressure distributions compared reasonably well with experimental data for all ramp angles. Numerical skin-friction distributions did not reproduce the postshock increase that appeared in measured results. A mesh resolution study indicated that coarse-grid simulations might be useful for practical applications, particularly for preliminary design purposes.

Although similar in shape, LES profiles of time-mean tangential velocity at specific streamwise locations only qualitatively resembled those of the experiments. The fluctuating component was in better agreement with the data for ramp angles of 16 and 20 deg. Numerical Reynolds stress profiles poorly predicted the experiment in all cases.

Comparisons with unsteady surface pressure measurements for the 24-deg ramp case were encouraging. Although it appeared that the numerically observed shock wave motion was somewhat different from that of the experiment, distributions of standard deviation, skewness, kurtosis, and intermittency were in correspondence with the data, except in the immediate vicinity of the mean separation point.

Acknowledgments

The work presented here was sponsored by the U.S. Air Force Office of Scientific Research under Task 2304IW and was monitored by R. Herklotz. Computational resources were supported in part

by a grant of supercomputer time from the U.S. Department of Defense Major Shared Resource Centers at Stennis Space Center, Mississippi, and Aberdeen Proving Ground, Maryland.

References

[1]Rai, M. M., Gatski, T. B., and Erlebacher, G., "Direct Simulation of Spatially Evolving Compressible Turbulent Boundary Layers," AIAA Paper 95-0583, Jan. 1995.

[2]Spyropoulos, E. T., and Blaisdell, G. A., "Large-Eddy Simulation of a Spatially Evolving Supersonic Turbulent Boundary-Layer Flow," *AIAA Journal*, Vol. 36, No. 11, 1998, pp. 1983–1990.

[3]Germano, M., Piomelli, U., Moin, P., and Cabot, W. H., "A Dynamic Subgrid-Scale Eddy Viscosity Model," *Physics of Fluids A*, Vol. 3, No. 7, 1991, pp. 1760–1765.

[4]Rizzetta, D. P., Visbal, M. R., and Gaitonde, D. V., "Direct Numerical and Large-Eddy Simulation of Supersonic Flows by a High-Order Method," AIAA Paper 2000-2408, June 2000.

[5]Guarini, S. E., Moser, R. D., Shariff, K., and Wray, A., "Direct Numerical Simulation of a Supersonic Turbulent Boundary Layer at Mach 2.5," *Journal of Fluid Mechanics*, Vol. 414, July 2000, pp. 1–33.

[6]Lee, S., Lele, S. V., and Moin, P., "Direct Numerical Simulation of Isotropic Turbulence Interacting with a Weak Shock Wave," *Journal of Fluid Mechanics*, Vol. 251, June 1993, pp. 533–562.

[7]Ducros, F., Ferrand, V., Nicoud, F., Weber, C., Darracq, D., Gacherieu, C., and Poinsot, T., "Large-Eddy Simulation of the Shock/Turbulence Interaction," *Journal of Computational Physics*, Vol. 152, No. 2, 1999, pp. 517–549.

[8]Andreopoulos, J., and Muck, K. C., "Some New Aspects of the Shock-Wave/Boundary-Layer Interaction in Compression-Ramp Flows," *Journal of Fluid Mechanics*, Vol. 180, July 1987, pp. 405–428.

[9]Smits, A. J., and Muck, K.-C., "Experimental Study of Three Shock Wave/Turbulent Boundary Layer Interactions," *Journal of Fluid Mechanics*, Vol. 182, Sept. 1987, pp. 291–314.

[10]Dolling, D. S., and Murphy, M. T., "Unsteadiness of the Separation Shock Wave Structure in a Supersonic Compression Ramp Flowfield," *AIAA Journal*, Vol. 21, No. 12, 1983, pp. 1628–1634.

[11]Dolling, D. S., and Or, C. T., "Unsteadiness of the Shock Wave Structure in Attached and Separated Compression Ramp Flows," *Experiments in Fluids*, Vol. 3, No. 1, 1985, pp. 24–32.

[12]Erengil, E. E., and Dolling, D. S., "Unsteady Wave Structure Near Separation in a Mach 5 Compression Ramp Interaction," *AIAA Journal*, Vol. 29, No. 5, 1990, pp. 728–735.

[13]Erengil, M. E., and Dolling, D. S., "Correlation of Separation Shock Motion with Pressure Fluctuations in the Incoming Boundary Layer," *AIAA Journal*, Vol. 29, No. 11, 1991, pp. 1868–1877.

[14]Settles, G. S., Fitzpatrick, T. J., and Bogdonoff, S. M., "Detailed Study of Attached and Separated Compression Corner Flowfields in High Reynolds Number Supersonic Flow," *AIAA Journal*, Vol. 17, No. 6, 1979, pp. 579–585.

[15]Hunt, D., and Nixon, D., "Very Large Eddy Simulation of an Unsteady Shock Wave/Turbulent Boundary Layer Interaction," AIAA Paper 95-2212, June 1995.

[16]Urbin, G., Knight, D., and Zheltovodov, A. A., "Compressible Large Eddy Simulation Using Unstructured Grid: Supersonic Turbulent Boundary Layer and Compression Corner," AIAA Paper 99-0427, Jan. 1999.

[17]Urbin, G., Knight, D., and Zheltovodov, A. A., "Large Eddy Simulation of a Supersonic Compression Corner Part I," AIAA Paper 2000-0398, Jan. 2000.

[18]Adams, N. A., "Direct Numerical Simulation of Turbulent Compression Ramp Flow," *Theoretical and Computational Fluid Dynamics*, Vol. 12, No. 2, 1998, pp. 109–129.

[19]Adams, N. A., "Direct Simulation of the Turbulent Boundary Layer Along a Compression Ramp at $M = 3$ and $Re_\theta = 1685$," *Journal of Fluid Mechanics*, Vol. 420, Oct. 2000, pp. 47–83.

[20]Rizzetta, D. P., Visbal, M. R., and Gaitonde, D. V., "Large-Eddy Simulation of Supersonic Compression-Ramp Flows by High-Order Method," *AIAA Journal*, Vol. 39, No. 12, 2001, pp. 2283–2292.

[21]Settles, G. S., and Dodson, L. J., "Hypersonic Shock/Boundary-Layer Interaction Database: New and Corrected Data," NASA CR-177638, April 1994.

[22]Yoshizawa, A., "Statistical Theory for Compressible Turbulent Shear Flows, with the Application to Subgrid Modeling," *Physics of Fluids*, Vol. 29, No. 7, 1986, pp. 2152–2164.

[23]Moin, P., Squires, W., Cabot, W., and Lee, S., "A Dynamic Subgrid-Scale Model for Compressible Turbulence and Scalar Transport," *Physics of Fluids A*, Vol. 3, No. 11, 1991, pp. 2746–2757.

[24]Beam, R., and Warming, R., "Implicit Factored Scheme for the Compressible Navier–Stokes Equations," *AIAA Journal*, Vol. 16, No. 4, 1978, pp. 393–402.

[25]Gordnier, R. E., and Visbal, M. R., "Numerical Simulation of Delta-Wing Roll," AIAA Paper 93-0554, Jan. 1993.

[26]Gaitonde, D., and Visbal, M. R., "High-Order Schemes for Navier–Stokes Equations: Algorithm and Implementation into FDL3DI," U.S. Air Force Research Lab., AFRL-VA-WP-TR-1998-3060, Wright–Patterson AFB, OH, Aug. 1998.

[27]Gordnier, R. E., and Visbal, M. R., "Numerical Simulation of Delta-Wing Roll," *Aerospace Science and Technology*, Vol. 2, No. 6, 1998, pp. 347–357.

[28]Gordnier, R. E., "Computation of Delta-Wing Roll Maneuvers," *Journal of Aircraft*, Vol. 32, No. 3, 1995, pp. 486–492.

[29]Visbal, M. R., "Computational Study of Vortex Breakdown on a Pitching Delta Wing," AIAA Paper 93-2974, July 1993.

[30]Visbal, M. R., "Onset of Vortex Breakdown Above a Pitching Delta Wing," *AIAA Journal*, Vol. 32, No. 8, 1994, pp. 1568–1575.

[31]Visbal, M., Gaitonde, D., and Gogineni, S., "Direct Numerical Simulation of a Forced Transitional Plane Wall Jet," AIAA Paper 98-2643, June 1998.

[32]Rizzetta, D. P., Visbal, M. R., and Stanek, M. J., "Numerical Investigation of Synthetic-Jet Flowfields," *AIAA Journal*, Vol. 37, No. 8, 1999, pp. 919–927.

[33]Rizzetta, D. P., Visbal, M. R., and Blaisdell, G. A., "Application of a High-Order Compact Difference Scheme to Large-Eddy and Direct Numerical Simulation," AIAA Paper 99-3714, June 1999.

[34]Steinbrenner, J. P., Chawner, J. P., and Fouts, C. L., "The GRIDGEN 3D Multiple Block Grid Generation System, Volume II: User's Manual," U.S. Air Force Wright Research and Development Center, WRDC-TR-90-3022, Feb. 1991.

[35]Rizzetta, D. P., and Visbal, M. R., "Large-Eddy Simulation of Supersonic Compression-Ramp flows," AIAA Paper 2001-2858, June 2001.

[36]Delery, J., and Marvin, J. G., "Shock-Wave/Boundary Layer Interactions," AGARDograph 280, edited by E. Reshotko, Feb. 1986.

[37]Delery, J. M., "Shock Wave/Turbulent Boundary Layer Interaction and Its Control," *Progress in Aerospace Sciences*, Vol. 22, No. 4, 1985, pp. 209–280.

[38]Ghosal, S., "Mathematical and Physical Constraints on Large-Eddy Simulation of Turbulence," *AIAA Journal*, Vol. 37, No. 4, 1999, pp. 425–433.

P. Givi
Associate Editor